Journal of
Advanced Manufacturing Science and Technology
jamst@jamstjournal.com；jamst2020@126.com
www.jamstjournal.com

A magnetically augmented eco-friendly conductive polymer composite for X-band electromagnetic interference shielding

Lingchong XUE, Hongze ZHANG, Zhiyuan ZHOU, Kedong BI*

Jiangsu Key Laboratory for Design and Manufacture of Micro-Nano Biomedical Instruments, School of Mechanical Engineering, Southeast University, Nanjing 211102, China

Received 10 May 2024; revised 17 June 2024; accepted 3 July 2024; Available online 12 July 2024

Abstract: Contemporary electronic device usage generates significant electromagnetic pollution, affecting nearby electronics and human health. Conventional shielding materials are inadequate, necessitating innovative solutions. This study developed a multilayered composite with iron(II, III) oxide (Fe_3O_4) nanoparticles, polythiophene (PTh) nanofiber arrays, and a gold nanolayer. The synergistic combination of magnetic nanoparticles and conductive polymer nanofiber arrays resulted in an electromagnetic interference (EMI) shielding effectiveness (SE) exceeding 30 dB in the X-band when Fe_3O_4 was used in moderate concentrations. This surpassed the EMI SE of a comparable composite prepared through a similar process but lacking Fe_3O_4 by approximately 10 dB. The enhanced EMI SE can be attributed to the magnetic nanoparticles, which introduced magnetic loss to attenuate electromagnetic radiation and improved the impedance match between the arrays and epoxy resin (EP) layers. Furthermore, the inclusion of nanoparticles enabled the material to exhibit an absorption-dominant EMI shielding mechanism, significantly reducing the secondary reflection of electromagnetic waves. Consequently, this novel eco-friendly EMI shielding composite shows promise for application in high-power electronic devices.

Keywords: conductive polymer composites; electromagnetic interference shielding; electropolymerization; nanofiber arrays; epoxy resin

1. Introduction

The contemporary pervasive utilization of devices such as smartphones, Wi-Fi routers, and Bluetooth devices engenders substantial EMI in the circumambient environment during operation. Moreover, electronics manufacturers prioritize the optimization of device miniaturization and the enhancement of processing speeds. The increased density of electronic components within individual devices has culminated in a marked increase in EMI generated by ubiquitous products such as mobile phones, liquid crystal display monitors, and laptop computers.[1] Consequently, electromagnetic pollution has emerged as the fourth most significant pollution issue after water, air, and noise pollution.[2] This interference compromises the normal function of proximal electronic devices and amplifies health risks including headaches, depression, and immunodeficiency populations routinely exposed to these emissions.[3-5] However, conventional EMI shielding materials such as metals possess several disadvantages, including high density, low elasticity, poor corrosion resistance, and exorbitant processing costs.[6] Furthermore, abundant surface reflection can propagate secondary electromagnetic wave contamination.[7] The development of novel EMI shielding coatings and devices to surmount these limitations is critical to sustain the proper operation of electronic devices and safeguard human health.[8-10]

In recent years, polymer-based EMI shielding materials have garnered incremental adoption as alternatives to conventional metallic shielding materials. This increased prevalence is attributable to polymeric substrates exhibiting favorable physicochemical properties, including low density, resistance to corrosion, cost-effectiveness, and facile processability.[11-14] However, the inherent insulating characteristics of many polymers limit their applicability in scenarios demanding significant EMI shielding performance, such as electronic devices, electric vehicles, medical instruments, and flexible printed circuit boards.[15, 16] To circumvent this limitation, researchers have incorporated fillers possessing high magnetic or electrical conductivity into polymer matrices to fabricate conductive polymer composites (CPC).[17] Compared to metallic materials, current CPC still suffers from drawbacks such as limited electrical conductivity and inferior EMI SE. Consequently, it is imperative to investigate methodologies for optimizing the EMI shielding performance of CPC through judicious structural design.[18]

In addition to the quantity and species of conductive fillers exerting a profound influence on the EMI shielding performance of CPC, the structural configuration of the composite and the spatial distribution of the conductive fillers within the polymer matrix are

* Corresponding author. *E-mail address:* kedongbi@seu.edu.cn(Kedong BI)
Peer review under responsibility of Editorial Committee of JAMST
DOI: 10.51393/j.jamst.2025004

equally consequential. Investigations have demonstrated that the structural design of EMI shielding materials plays a critical role in determining their effectiveness.[19] The fabrication of multiple interfaces has been proven as an efficacious approach to enhancing the EMI SE of CPC, including porous CPC, segregated CPC, multiphase CPC, multilayered CPC, and CPC with prefabricated conductive networks.[20] Multiple interfaces in CPC are recognized to augment shielding performance through mechanisms such as interfacial polarization, multiple reflection, interfacial dielectric loss, and interfacial electronic resonance. [21-23] Multilayered CPC is particularly advantageous, as they facilitate the controlled distribution of conductive fillers with multiple interfaces.[24, 25] This enables the formation of reliable conductive pathways and multiple reflection at interfaces, resulting in significant absorption loss of electromagnetic waves. [26-28] Even with a relatively low loading of conductive fillers, multilayered CPC demonstrate superior EMI shielding properties compared to conventional counterparts. [29] Common fabrication techniques for multilayered EMI shielding CPC films include vacuum filtration, coating, and polymer-assisted methods. [30-32] The coating method is employed to synthesize EMI shielding CPC films by curing a hybrid system comprising conductive fillers and a resin matrix in an appropriate mold. This simplistic method is widely utilized for practical manufacturing. Furthermore, prefabricated conductive networks can be fabricated by directing the conductive filler into a specific three-dimensional configuration within the resin matrix using lyophilization, hydrothermal synthesis, chemical vapor deposition, pyrolysis-carbonization, and template-based techniques.[33, 34] These prefabricated networks provide stable conductive frameworks that are not disrupted by the low viscosity polymer matrix during filling, leading to rapid enhancement of EMI SE at low filler loadings.[35, 36] Combining the coating method with template-based techniques allows for the preparation of multilayered EMI shielding CPC with prefabricated conductive networks.

In general, there exist two predominant approaches for fabricating polymer nanostructures: template-based and template-free methodologies.[37] The hard template technique represents the most prevalent and efficacious means of synthesizing highly regulated and oriented nanostructures. This approach utilizes either chemical polymerization or electrochemical polymerization, with the latter being more readily modulated by varying the current density, applied potential, and polymerization duration.[38] Vertically aligned PTh nanofiber arrays, with exceptional environmental stability and structural versatility, have been successfully synthesized utilizing nanoporous anodic aluminum oxide (AAO) with gold plating on one surface as a hard template.[39-45] Fe_3O_4 nanoparticles possess exceptional magnetic loss properties with respect to electromagnetic waves and have been extensively utilized as electromagnetic wave absorbers for EMI shielding CPC.[46] However, due to their relatively poor electrical conductivity, Fe_3O_4 nanoparticles tend to diminish the dielectric loss of EMI shielding CPC. Therefore, it is imperative to integrate them with conductive fillers to achieve heightened EMI shielding performance.[47]

In this study, we developed novel multilayered Carbon-Polymer Composites with pre-fabricated conductive networks through the integration of electrochemical hard templating and coating methodologies. By incorporating Fe_3O_4 magnetic nanoparticles onto PTh nanofibers, we significantly augmented the Electromagnetic Interference Shielding Effectiveness (EMI SE) of the composite within the X-band. Concurrently, we observed a notable increase in absorption loss, contributing to the composite's enhanced environmental friendliness. Subsequently, we elucidated the mechanism through which the composite attenuates EMI, providing insights for the rational design of EMI shielding CPC structures.

2. Experimental section

2.1. Materials

The nanoporous AAO utilized was procured from Hefei Jinghui Nanotechnology Co. and possessed nominal pore diameters of approximately 90 nm and a thickness of 100 μm. Gold evaporation sources (Au, 99.999%) were acquired from Beijing Purui New Material Technology Co. The EP E-51 and its curing agent set (YT-CC302Q) were obtained from Kunshan Yituo Composites Co. An aqueous dispersion of Fe_3O_4 nanoparticles (I812059) encompassing particle diameters ranging from 10 to 30 nm and a concentration of 25wt% was purchased from Shanghai Macklin Reagent Co. Unless otherwise specified, all other chemical reagents employed in this study were obtained from Shanghai Aladdin Biochemical Technology Co. and utilized as received.

2.2. Synthesis route

The multilayered EMI shielding CPC with prefabricated conductive networks was fabricated via a meticulously designed multi-stage process, in which the EP was situated within the upper and lower strata. Interposed was a multilayered nanocomposite membrane composed of Fe_3O_4 nanoparticles, PTh nanofiber arrays, and an Au layer. As depicted in Fig. 1, the procedure for synthesizing this EMI shielding composite consisted of five stages: electropolymerization, membrane attachment, chemical etching, dispersion immersion, and coating.

Before electrochemical deposition, one surface of the AAO template needed to be transformed into an electrode to facilitate the synthesis of PTh within the nanochannels. As a result, a 50 nm thick layer of gold was evaporated onto one side of the template in a high vacuum environment at 5×10^{-4} Pa to 8×10^{-4} Pa. The gold layer served as the working electrode for electro-polymerization, facilitating the direct growth of PTh nanofibers. This process was achieved through electrochemical oxidation at a consistent potential of 1.5 V relative to Ag/AgCl, utilizing a three-electrode one-compartment cell equipped with a computer-controlled potentiostat-galvanostat (CH Instruments electrochemical system, CHI660E) for 50 minutes. The schematic of the electrochemical cell utilized for fabricating the polythiophene nanofiber arrays is presented in Fig. 2. Within this cell, PTh nanofibers were synthesized electrochemically via electrolysis with 0.03 mol/L thiophene in boron fluoride diethyl ether (98%). During the process of electrosynthesis of the PTh nanofiber arrays, a clean and polished stainless steel (AISI 304) sheet slightly oversizing the AAO template was utilized as the counter electrode,[40] while an Ag/AgCl electrode immersed directly within the solution functioned as the reference electrode. All solutions were deoxygenated with high-purity argon, and a slight positive pressure of argon was maintained during fiber development. [45] The composite of PTh nanofibers and the AAO template was washed repeatedly with anhydrous ethanol and deionized water subsequent to electropolymerization.

The secondary stage entails securing the film, which is imperative for maintaining the integrity of the film during etching to preclude rupture due to inadequate mechanical robustness. This signifies that the composite of the template and fibers is positioned on the uncured EP such that the gold surface adheres firmly to the EP as it cures. In other words, the PTh nanofiber arrays in conjunction

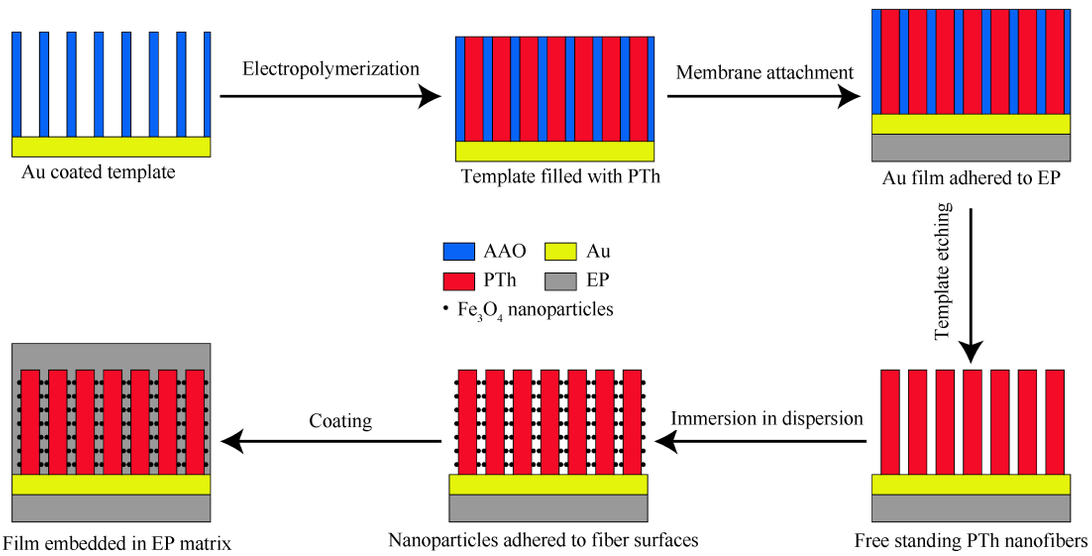

Fig. 1. Synthesis route of Fe_3O_4/PTh/Au/EP multilayered EMI shielding CPC with prefabricated conductive networks.

with the AAO template were affixed to the EP layer via the adhesion between the gold layer and the EP. This is attributable to the AAO template purchased encompassing a protective ring of high-purity aluminum, which will react with potassium hydroxide (KOH) to evolve hydrogen gas during chemical etching. The substantial quantity of bubbles will compromise the fiber film and induce rupture. As for the detailed preparatory methodology and process parameters, EP and its cure agents were mixed at a mass ratio of 1:3, agitated thoroughly, and allowed to stand for 10 minutes to eliminate air bubbles. Subsequently, approximately 7 g of EP was dispensed into a 90 mm diameter mold to completely cover the floor of the mold. The mold was then situated on a flat surface such that the EP was uniformly distributed across the floor of the mold. The high-purity aluminum situated at the periphery of the AAO template was trimmed to enable the AAO template to rest flatly within the mold. The gold surface of the template with PTh nanofibers was oriented face down on the uncured EP, and the EP was permitted to cure for 24 hours.

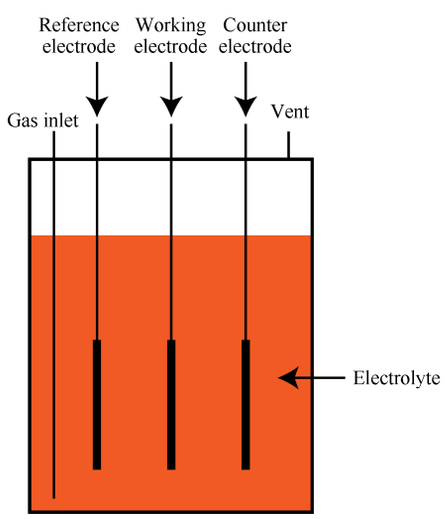

Fig. 2. Schematic of three-electrode one-compartment electrochemical cell used for electropolymerization.

The subsequent stage encompasses chemical etching. To liberate the PTh nanofiber arrays aligned vertically, the template was treated with 1 mol/L KOH for 24 hours and subsequently rinsed thoroughly with deionized water and anhydrous ethanol prior to further processing. Thereafter, the composite was immersed in a dispersion of Fe_3O_4 nanoparticles diluted to 1.25wt% for 4 hours to facilitate the nanoparticles to adsorb onto the surfaces of the nanofibers, before being extracted from the dispersion and dehydrated in a blast drying oven at 40 °C. Employing an identical methodology and parameters as previously described, an EP coating was overlaid above the arrays, ultimately resulting in the fabrication of the Fe_3O_4/PTh/Au/EP composite with a thickness of approximately 2.5 mm.

2.3. Characterization

X-ray diffraction (XRD) analyses were performed utilizing Cu Kα radiation with an X-ray diffractometer (Smartlab (3), Rigaku Co., Ltd., Japan). Scanning electron microscopy (SEM) images were acquired using an FEI Inspect F50 field-emission scanning electron microscope (Thermo Fisher Scientific Co.) at an accelerating voltage of 20 kV. Before SEM imaging, the sample was sputter-coated with gold to enhance its electrical conductivity.[48] Raman spectra were obtained using a WITec alpha300 RA microscope (Oxford Instruments plc) equipped with a 633 nm excitation laser with optical power below 0.7 mW to preclude sample degradation.[49] EMI shielding parameters were determined via a vector network analyzer (VNA, Ceyear 3656D, Ceyear Technologies Co., Ltd.). Electrical conductivity was calculated from the measured resistivity using a four-point probe (Model HPS2661, Helpass Electronic Technologies, Inc.).

3. Presentation of results

Fig. 3 illustrates the SEM images of the PTh nanofiber arrays before and after the inclusion of Fe_3O_4 nanoparticles. Figs. 3(a)-(c) display SEM images of the PTh nanofiber arrays in the absence of Fe_3O_4 nanoparticles at 1000×, 3000×, and 160000× magnification, respectively. As evident in Fig. 3(a), while certain fibers do not remain strictly perpendicular following the removal of the template due to insufficient rigidity, the majority of the PTh nanofibers are aligned vertically in a relatively orderly fashion, forming arrays of large domains with high density. Figs. 3(b)-(c) demonstrate that the nanofibers have adhered uniformly and securely to the gold film, with lengths of approximately 20 μm and diameters of roughly 85

nm, which is marginally smaller than the pore size of the AAO template. This phenomenon can be attributed to the fact that the pore diameters of the template govern the nanofiber diameters, which remain relatively homogeneous despite irregularities in the template that result in fluctuations of these diameters.[45] Given that deposition was conducted at a constant potential, the nanofiber lengths are determined by the electropolymerization duration and rate, with longer deposition periods yielding longer nanofibers until the template thickness is attained.[40] The rate of electrochemical deposition is governed by the current density during the reaction, particularly in constant potential mode, which is primarily influenced by the solution concentration, electrode conductivity, and the applied potential. The morphology of the nanofiber arrays following the inclusion of Fe_3O_4 nanoparticles is depicted in Fig. 3(d). A comparison of Fig. 3(d) with SEM images prior to nanoparticle addition reveals successful deposition onto the nanofibers. This success can be attributed to the favorable adhesion properties of the PTh nanofibers, enabling secure attachment of magnetic nanoparticles to the nanofiber surfaces without the need for surfactants.[43, 44, 50]

As evidenced in Fig. 4, the XRD spectrum of the pristine EP E-51 exhibits a broad peak centered at 20°, which arises from the amorphous characteristic peak of the EP.[51] Analogously, the XRD patterns of PTh/Au/EP and Fe_3O_4/PTh/Au/EP demonstrate characteristic peaks at approximately 20°, corresponding not solely to the amorphous characteristic peaks of the EP but also to the amorphous characteristic peaks of PTh. According to previous studies, the semi-crystalline PTh could be obtained via electropolymerization at a constant current, whereas the amorphous PTh could be obtained via electropolymerization at a constant potential.[45] The peaks appearing at 38°, 44°, 65° and 78° in Fe_3O_4/PTh/Au/EP and PTh/Au/EP can be attributed to the diffraction planes (111), (200), (220) and (311) of gold.[52] The diffraction peaks at 30°, 36°, 57° and 63° correlate to the (220), (311), (440), and (511) crystal planes of Fe_3O_4, present in Fe_3O_4/PTh/Au/EP.[19, 52] As the composite become more complex, the characteristic peaks of both the added component (i.e. Fe_3O_4) and the initial component become less distinct, resulting in certain peaks being challenging to identify unambiguously. Nevertheless, the majority of the characteristic peaks of Fe_3O_4 confirm the presence of Fe_3O_4 in the composite. This indicates the successful incorporation of Fe_3O_4 into the PTh/Au/EP composite.

The molecular architectures of the PTh nanofibers and Fe_3O_4/PTh composite were investigated through Raman spectroscopic analyses. The Raman spectra depicted in Fig. 5 were obtained by focusing the laser excitation beam on the surface of the specimens under study. The most intense vibrational band in the Raman spectrum of the PTh nanofibers was located at ca. 1456 cm^{-1}, which can be attributed to the symmetric stretching vibration of the aromatic C=C bond within the ring, associated with neutral conjugated PTh segments.[45, 53] Two additional substantially weaker bands at 1045 cm^{-1} (C-H bending) and 703 cm^{-1} (C-S-C ring bending) were also observed, which correlate with oxidized PTh or structural defects.[45, 53] In the Raman spectra of the Fe_3O_4/PTh composite, the most prominent band was assigned to PTh, at 1456 cm^{-1}, while three other major Raman bands were detected at around 365, 512, and 671 cm^{-1}, corresponding to the E_g, $T_{2g}(2)$, and A_{1g} vibrational modes of Fe_3O_4, respectively.[49, 54, 55] However, due to the poor signal-to-noise ratio and interference from the PTh signal, these bands exhibited minor shifts relative to the standard Raman bands of Fe_3O_4, particularly the E_g mode which demonstrated a blue shift of approximately 50 cm^{-1}.

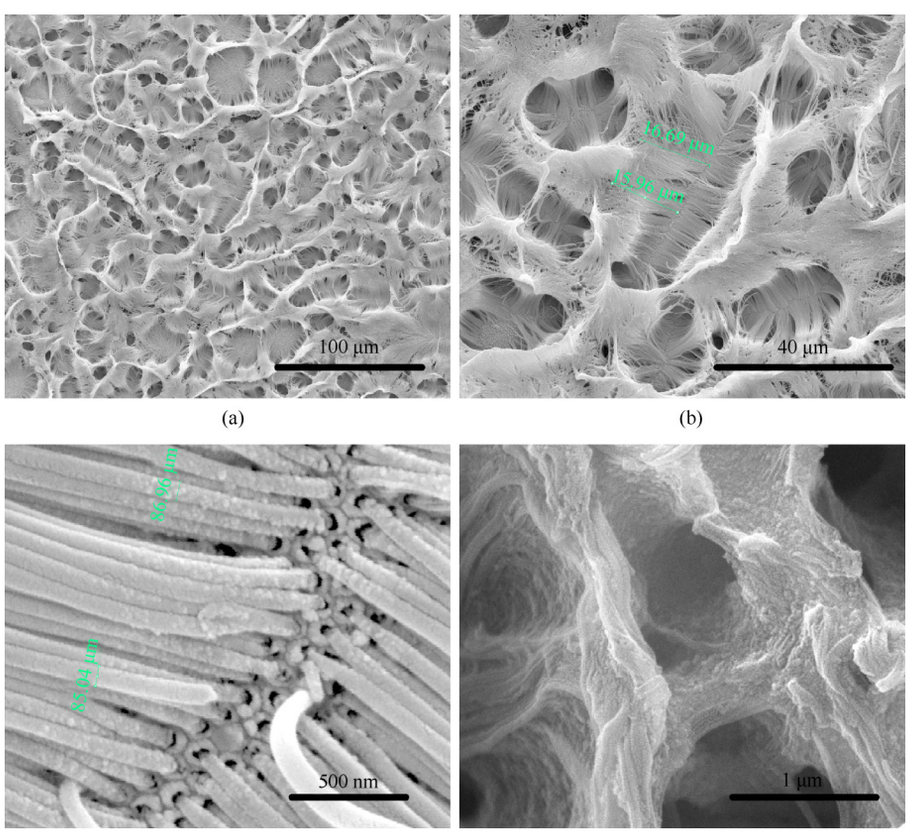

(a) (b) (c) (d)

Fig. 3. (a-c) SEM images of PTh nanofiber arrays, (d) SEM images of Fe_3O_4 nanoparticles adhered to PTh nanofiber arrays.

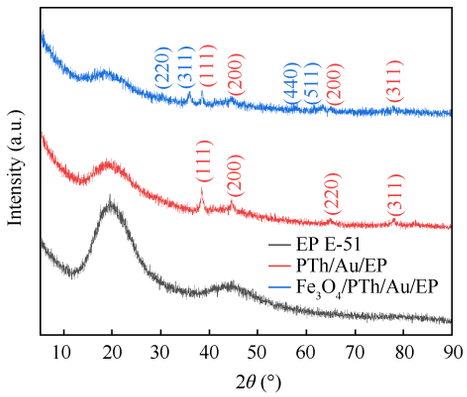

Fig. 4. XRD spectra of EP E-51, PTh/Au/EP, and Fe_3O_4/PTh/Au/EP, where red diffraction plane labels signify that they correspond to diffraction planes of Au and the blue diffraction plane labels signify that they are from Fe_3O_4.

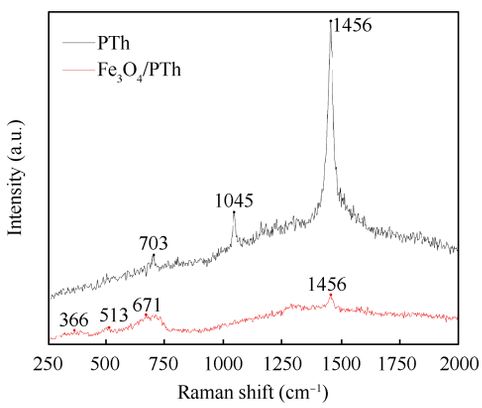

Fig. 5. Raman spectra of PTh nanofibers and Fe_3O_4/PTh.

Fig. 6 depicts the hysteresis loops of PTh/Au/EP and Fe_3O_4/PTh/Au/EP measured at ambient temperature. As evidenced in the figure, the measured saturation magnetization (M_s) prior to and subsequent to the addition of magnetic nanoparticles was 5.95 × 10^{-3} and 7.24 × 10^{-2} emu/g, respectively, and the measured remanent magnetization (M_r) was 2.40×10^{-5} and 7.01×10^{-4} emu/g, respectively. The calculated squareness ratios (M_r/M_s) were 4.04×10^{-3} and 9.67×10^{-3}, and the measured coercive forces (H_c) were 7.22 and 13.23 Oe, respectively. Based on the H_c, we can speculate that the measured specimens are soft magnetic materials. The M_s of the specimens is low, which can be attributed to the fact that the majority of the specimens comprise non-magnetic EP. After the addition of magnetic nanoparticles, the M_s of the specimens increased substantially.

As evidenced in Fig. 7, the average electrical conductivity of PTh/Au was approximately 227 S/m with a standard deviation of 12 S/m, indicating the successful formation of an adequate conductive network. In contrast, the average conductivity of Fe_3O_4/PTh/Au exhibited a negligible increase to 239 S/m after the addition of Fe_3O_4 nanoparticles, which may primarily result from the poor conductivity of the added Fe_3O_4 nanoparticles themselves. Although the standard deviation of the conductivity increased with the incorporation of nanoparticles, the error remained within an acceptable range. This suggests that while the introduction of nanoparticles amplifies the inhomogeneity within the film, they adhere to the nanofiber surface in a relatively uniform manner, resulting in a generally homogeneous distribution of conductivity throughout the nanofilm.

Fig. 8 illustrates the EMI SE of typical EP E-51, PTh/Au/EP, and

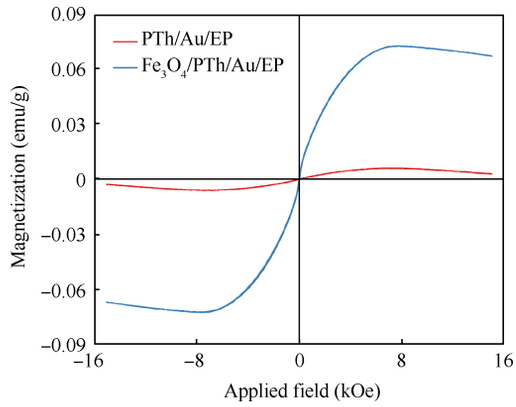

Fig. 6. Hysteresis loops of PTh/Au/EP and Fe_3O_4/PTh/Au/EP.

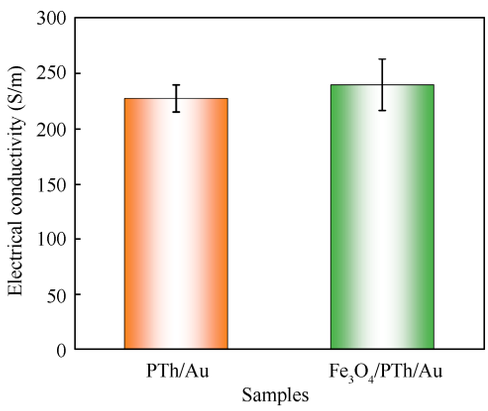

Fig. 7. Electrical conductivity of PTh/Au and Fe_3O_4/PTh/Au.

Fe_3O_4/PTh/Au/EP specimens within the X-band frequency range. As shown in Figs. 8(a)-(d), the EP sheet exhibited negligible EMI shielding capability (~1.5 dB). Upon the incorporation of the PTh/Au nanofilm, the total shielding effectiveness (SE_T) of PTh/Au/EP improved substantially to approximately 24 dB, which satisfies commercial requirements (SE_T > 20 dB) but remains within the classification of a low-level EMI shielding material (10-30 dB) suitable only for rudimentary shielding applications.[17, 19] When electromagnetic radiation is incident upon the PTh/Au/EP surface, it first encounters the EP layer, which possesses negligible shielding capacity, enabling the electromagnetic waves to traverse the EP layer with slight loss to interact with the PTh nanofiber arrays. Although PTh is a conjugated polymer where π-π stacking interactions result in polarization loss[56, 57], most incident microwaves penetrate the PTh layer and interact with the gold layer with minor loss due to the impedance matching between PTh and EP[58], indicating the nanoarray structure provides negligible contribution. The impedance matching can be primarily attributed to the poor conductivity and absence of magnetism in semiconducting PTh, which yields comparable complex permittivity and permeability.[59] Therefore, the EMI shielding properties of the PTh/Au/EP composite originate primarily from the gold layer. The excellent electrical conductivity of gold induces a significant impedance mismatch between PTh and gold, resulting in the reflection of most electromagnetic radiation incident upon the gold surface. The minority of electromagnetic waves penetrating the gold layer undergo dielectric loss, including polarization loss from interfacial polarization and relaxation, and ohmic loss from microcurrents via charge carriers.[60, 61] Polarization loss in PTh and dielectric loss in the gold layer constitute the primary sources of absorption shielding effectiveness (SE_A) in the PTh/

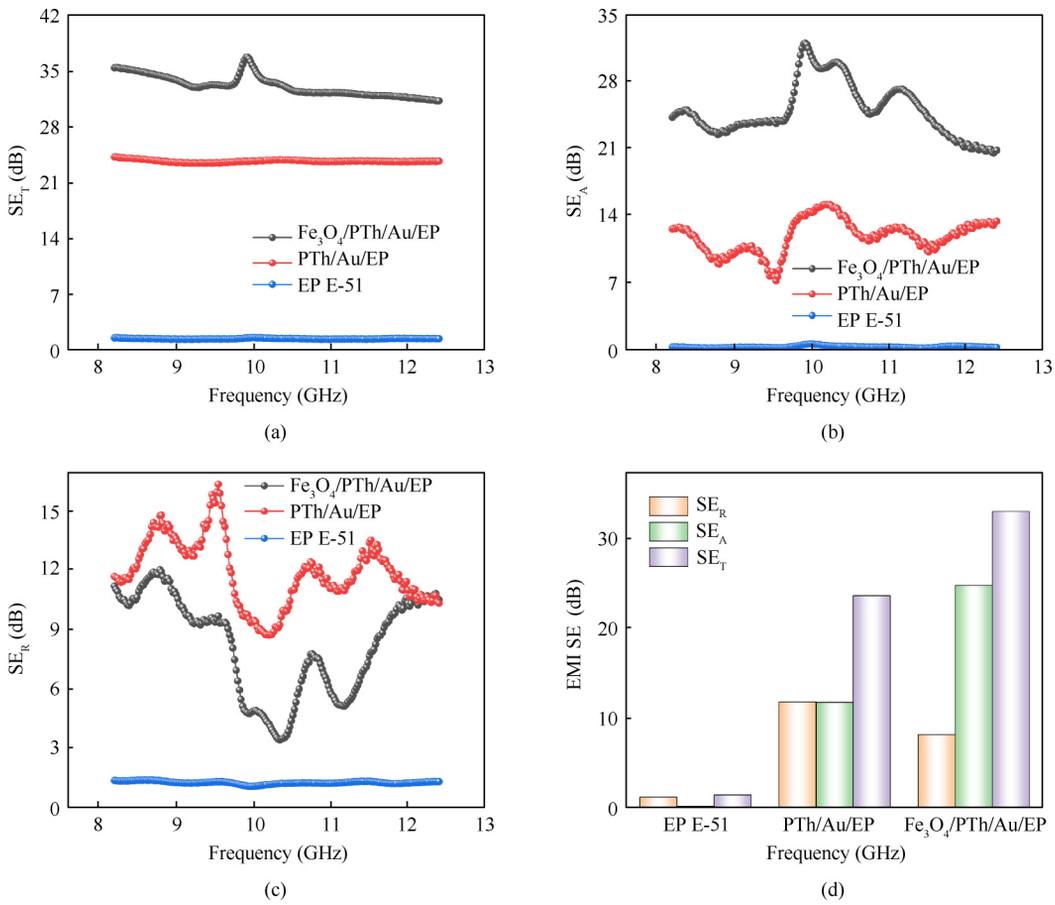

Fig. 8. (a-c) SE_T, SE_A, and SE_R of typical EP E-51, PTh/Au/EP, and Fe_3O_4/PTh/Au/EP specimens within X-band frequency range, (d) comparison charts of EMI SE of typical EP E-51, PTh/Au/EP, and Fe_3O_4/PTh/Au/EP specimens within the X-band frequency range.

Au/EP composite. As shown in Fig. 8(d), the reflection shielding effectiveness (SE_R) of PTh/Au/EP is comparable to the SE_A. Although the EMI shielding performance of the PTh/Au/EP composite satisfies commercial requirements, the substantial reflection may lead to secondary environmental pollution from electromagnetic radiation. Furthermore, certain limitations exist in the structural design of the PTh/Au/EP composite, introducing constraints on their EMI shielding performance. Optimization of the PTh/Au/EP structural design to enhance the absorption is, therefore, necessary to fulfill environmental friendliness requirements and improve EMI shielding performance.

Upon incorporation of Fe_3O_4 nanoparticles exhibiting inferior electrical conductivity yet superior magnetic properties, an impedance mismatch transpired between the nanoarrays and the EP matrix. The majority of incident microwaves were reflected at the nanoparticle-EP interface, propagating repeated reflection across the multi-interfacial nanoarray geometry, thereby eliciting severe multiple reflection loss. Moreover, the introduction of magnetic nanoparticles led to a predominant magnetic loss, primarily attributed to natural resonance phenomena.[62] Magnetic materials possessing enhanced anisotropy commonly display elevated natural resonance frequencies.[63] In this study, the embedded magnetic nanoparticles exhibited substantial natural resonance effects due to their high saturation magnetization and anisotropy arising from the one-dimensional nanofiber arrays. Consequently, the SE_T of the Fe_3O_4/PTh/Au/EP increased markedly to approximately 33 dB, fulfilling the criteria for intermediate EMI shielding materials (30-60 dB) and addressing most industrial shielding requirements.[17] This synergistic combination of magnetic nanoparticles and conductive polymer nanofiber arrays resulted in a superior EMI shielding performance than carbon-based polymer somposites (about 20 dB[64-66]) and ferrite added to other polymer composites.[67, 68] Furthermore, Figs. 8(b)-(d) illustrates that upon nanoparticle addition, the SE_A intensified as the SE_R diminished, with the former exceeding the latter significantly. This signifies an absorption-dominated EMI shielding mechanism after optimization.[19] These findings suggest that the composite meets the criteria for environmentally friendly EMI shielding materials and effectively mitigates secondary pollution from electromagnetic radiation in the surrounding environment.

We further investigated the absorption-dominated EMI shielding mechanism of this CPC from a microstructural perspective. As a prefabricated conductive network, the EMI shielding nanocomposite film comprises two strata: the upper magnetic array layer encompassing Fe_3O_4 magnetic nanoparticles enveloping PTh nanofiber arrays, and the lower gold conductive layer. The EMI shielding nanocomposite film is encased within EP on its upper and lower surfaces, constituting a multilayered EMI shielding CPC. As illustrated in Fig. 9, upon the incidence of an electromagnetic wave on the surface of the composite, it initially encounters the EP matrix, which possesses almost no shielding capacity. Consequently, the electromagnetic waves propagate through the EP layer to reach the magnetic array layer. Owing to impedance mismatch between the magnetic nanoparticles and the EP, the majority of incident electromagnetic waves undergo reflection at the nanoparticle-EP interface.

This is followed by multiple reflections within the arrays, leading to considerable losses due to multiple reflections, along with magnetic losses primarily caused by natural resonance. The magnetic loss mechanisms of magnetic materials predominantly originate from hysteresis, domain wall resonance, natural ferromagnetic resonance, and eddy currents.[69-72] The hysteresis loss is negligible under weak magnetic fields, whereas the domain wall resonance loss typically transpires at substantially lower frequencies (MHz order).[73] Due to the impedance mismatch between magnetic nanoparticles, Pth, and Au, electromagnetic waves traversing the interface will reflect partially. Therefore, numerous electromagnetic waves will undergo repetitive multiple reflection loss and magnetic loss. The electromagnetic waves pervading the gold layer will experience identical dielectric loss as that in the gold layer of the PTh/Au/EP composite. The multiple reflection loss, dielectric loss, and magnetic loss constitute the primary electromagnetic wave absorption mechanisms, which can effectively minimize electromagnetic wave reflection and mitigate secondary electromagnetic pollution of the ambient environment.

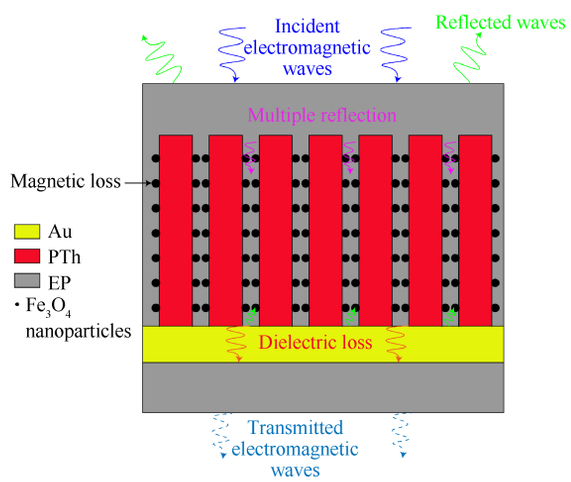

Fig. 9. Schematic diagram of EMI shielding mechanism of the Fe_3O_4/PTh/Au/EP composite.

4. Conclusions

In summary, we employed the electrochemical hard-template technique to construct vertically aligned arrays of PTh nanofibers. This structural design increases the number of interfaces, facilitating enhanced multiple reflections of electromagnetic waves. The multilayered architecture of the magnetic and conductive layers allows for repetitive reflection of electromagnetic waves within the nano-composite film, thereby amplifying the dielectric and magnetic loss of the EMI shielding composite against incident electromagnetic waves. By incorporating magnetic nanoparticles to optimize the impedance mismatch at the array surfaces, our multilayered EMI shielding composite achieves an EMI SE of approximately 33 dB, a significant improvement compared to the counterpart lacking magnetic nanoparticle integration (approximately 24 dB). This innovative and environmentally friendly EMI shielding composite exhibits proficient absorption-dominated EMI shielding properties, making it a promising material for high-power device applications.

Acknowledgments

This work was financially supported by the National Natural Science Foundation of China (51975120) and Qing Lan Project of Colleges and Universities of Jiangsu Province.

References

1. Yang Z, Peng H, Wang W, et al. Crystallization behavior of poly(ε-caprolactone)/layered double hydroxide nanocomposites. *Journal of Applied Polymer Science* 2010; 116 (5): 2658-2667.
2. Balmori A. Electromagnetic pollution from phone masts: Effects on wildlife. *Pathophysiology* 2009; 16 (2): 191-199.
3. Thomassin J-M, Jérôme C, Pardoen T, et al. Polymer/carbon based composites as electromagnetic interference (EMI) shielding materials. *Materials Science and Engineering: R: Reports* 2013; 74 (7): 211-232.
4. Shahzad F, Alhabeb M, Hatter CB, et al. Electromagnetic interference shielding with 2D transition metal carbides (MXenes). *Science* 2016; 353 (6304):1137-1140.
5. Abbasi H, Antunes M, Velasco JI. Recent advances in carbon-based polymer nanocomposites for electromagnetic interference shielding. *Progress in Materials Science* 2019; 103: 319-373.
6. Wanasinghe D, Aslani F, Ma G, et al. Review of polymer composites with diverse nanofillers for electromagnetic interference shielding. *Nanomaterials* 2020; 10 (3): 541.
7. Ji H, Zhao R, Zhang N, et al. Lightweight and flexible electrospun polymer nanofiber/metal nanoparticle hybrid membrane for high-performance electromagnetic interference shielding. *NPG Asia Materials* 2018; 10(8), 749-760.
8. Song W, Guan X, Fan L, et al. Tuning three-dimensional textures with graphene aerogels for ultra-light flexible graphene/texture composites of effective electromagnetic shielding. *Carbon* 2015; 93:151-160.
9. Song W, Cao M, Lu M, et al. Flexible graphene/polymer composite films in sandwich structures for effective electromagnetic interference shielding. *Carbon* 2014; 66:67-76.
10. Tan Y, Li J, Gao Y, et al. A facile approach to fabricating silver-coated cotton fiber non-woven fabrics for ultrahigh electromagnetic interference shielding. *Applied Surface Science* 2018; 458:236-244.
11. Gao L, Li C, Huang W, et al. MXene/polymer membranes: synthesis, properties, and emerging applications. *Chemistry of Materials* 2020; 32 (5): 1703-1747.
12. Pang Y, Yang Z, Yang Y, et al. Wearable electronics based on 2D materials for human physiological information detection. *Small* 2020; 16 (15): 1901124.
13. Kumar P, Narayan Maiti U, Sikdar A, et al. Recent advances in polymer and polymer composites for electromagnetic interference shielding: Review and future prospects. *Polymer Reviews* 2019; 59 (4): 687-738.
14. Wu L, Wu F, Sun Q, et al. A TTF-TCNQ complex: an organic charge-transfer system with extraordinary electromagnetic response behavior. *Journal of Materials Chemistry C* 2021; 9 (9): 3316-3323.
15. Jiang D, Murugadoss V, Wang Y, et al. Electromagnetic interference shielding polymers and nanocomposites - A review. *Polymer Reviews* 2019; 59 (2): 280-337.
16. Guo M, Huang J, Deng Y, et al. pH-responsive cyanine-grafted graphene oxide for fluorescence resonance energy transfer-enhanced photothermal therapy. *Advanced Functional Materials* 2015; 25 (1): 59-67.
17. Liang C, Gu Z, Zhang Y, et al. Structural design strategies of polymer matrix composites for electromagnetic interference shielding: A review. *Nano-Micro Letters* 2021; 13 (1): 181.
18. Singh AK, Shishkin A, Koppel T, et al. A review of porous lightweight composite materials for electromagnetic interference shielding. *Composites Part B: Engineering* 2018; 149: 188-197.
19. Zhang Y, Ruan K, Gu J. Flexible sandwich-structured electromagnetic interference shielding nanocomposite films with excellent thermal conductivities. *Small* 2021; 17 (42): 2101951.
20. Wang M, Tang X-H, Cai J-H, et al. Construction, mechanism and prospective of conductive polymer composites with multiple interfaces for electromagnetic interference shielding: A review. *Carbon* 2021; 177: 377-402.
21. Gao W, Zheng Y, Shen J, et al. Electrical properties of polypropylene-

based composites controlled by multilayered distribution of conductive particles. *ACS Applied Materials & Interfaces* 2015; 7(3): 1541-1549.
22. Zhang Y, Yang Z, Pan T, et al. Construction of natural fiber/polyaniline core-shell heterostructures with tunable and excellent electromagnetic shielding capability via a facile secondary doping strategy. *Composites Part A: Applied Science and Manufacturing* 2020; 137:105994.
23. Gao W, Zhao N, Yu T, et al. High-efficiency electromagnetic interference shielding realized in nacre-mimetic graphene/polymer composite with extremely low graphene loading. *Carbon* 2020; 157: 570-577.
24. Poothanari MA, Abraham J, Kalarikkal N, et al. Excellent electromagnetic interference shielding and high electrical conductivity of compatibilized polycarbonate/polypropylene carbon nanotube blend nanocomposites. *Industrial & Engineering Chemistry Research* 2018; 57 (12): 4287-4297.
25. Xia C, Yu J, Shi SQ, et al. Natural fiber and aluminum sheet hybrid composites for high electromagnetic interference shielding performance. *Composites Part B: Engineering* 2017; 114: 121-127.
26. Wang Y, Cheng X-D, Song W-L, et al. Hydro-sensitive sandwich structures for self-tunable smart electromagnetic shielding. *Chemical Engineering Journal* 2018; 344:342-352.
27. He L, Shi Y, Wang Q, et al. Strategy for constructing electromagnetic interference shielding and flame retarding synergistic network in poly (butylene succinate) and thermoplastic polyurethane multilayered composites. *Composites Science and Technology* 2020; 199: 108324.
28. Hu Y, Li D, Wu L, et al. Carbon nanotube buckypaper and buckypaper/polypropylene composites for high shielding effectiveness and absorption-dominated shielding material. *Composites Science and Technology* 2019; 181:107699.
29. Tang X-H, Li J, Wang Y, et al. Controlling distribution of multi-walled carbon nanotube on surface area of Poly(ε-caprolactone) to form sandwiched structure for high-efficiency electromagnetic interference shielding. *Composites Part B: Engineering* 2020; 196: 108121.
30. Liu J, Liu Z, Zhang H-B, et al. Ultrastrong and highly conductive MXene-based films for high-performance electromagnetic interference shielding. *Advanced Electronic Materials* 2020; 6 (1): 1901094.
31. Luo J-Q, Zhao S, Zhang H-B, et al. Flexible, stretchable and electrically conductive MXene/natural rubber nanocomposite films for efficient electromagnetic interference shielding. *Composites Science and Technology* 2019; 182: 107754.
32. Ma Z, Kang S, Ma J, et al. High-performance and rapid-response electrical heaters based on ultraflexible, heat-resistant, and mechanically strong aramid Nanofiber/Ag nanowire nanocomposite papers. *ACS Nano* 2019; 13 (7): 7578-7590.
33. Li X-H, Li X, Liao K-N, et al. Thermally annealed anisotropic graphene aerogels and their electrically conductive epoxy composites with excellent electromagnetic interference shielding efficiencies. *ACS Applied Materials & Interfaces* 2016; 8 (48): 33230-33239.
34. Chen Y, Zhang H-B, Huang Y, et al. Magnetic and electrically conductive epoxy/graphene/carbonyl iron nanocomposites for efficient electromagnetic interference shielding. *Composites Science and Technology* 2015; 118: 178-185.
35. Liang C, Song P, Qiu H, et al. Constructing interconnected spherical hollow conductive networks in silver platelets/reduced graphene oxide foam/epoxy nanocomposites for superior electromagnetic interference shielding effectiveness. *Nanoscale* 2019; 11 (46): 22590-22598.
36. Liang C, Qiu H, Han Y, et al. Superior electromagnetic interference shielding 3D graphene nanoplatelets/reduced graphene oxide foam/epoxy nanocomposites with high thermal conductivity. *Journal of Materials Chemistry C* 2019; 7 (9): 2725-2733.
37. Abdelhamid ME, O'Mullane AP, Snook GA. Storing energy in plastics: a review on conducting polymers & their role in electrochemical energy storage. *RSC Advances* 2015; 5 (15): 11611-11626.
38. Xia L, Wei Z, Wan M. Conducting polymer nanostructures and their application in biosensors. *Journal of Colloid and Interface Science* 2010; 341 (1): 1-11.
39. Fu M, Chen F, Zhang J, et al. Electrochemical fabrication of aligned microtubular heterojunctions of poly(p-phenylene) and polythiophene. *Journal of Materials Chemistry* 2002; 12 (8): 2331-2333.
40. Zhang J, Shi G, Liu C, et al. Electrochemical fabrication of polythiophene film coated metallic nanowire arrays. *Journal of Materials Science* 2003; 38 (11): 2423-2427.
41. Zhang Z, Qu L, Shi G. Fabrication of highly hydrophobic surfaces of conductive polythiophene. *Journal of Materials Chemistry* 2003; 13 (12): 2858-2860.
42. Cao J, Sun J, Shi G, et al. Photovoltaic properties of polythiophene nano-tubule films. *Materials Chemistry and Physics* 2003; 82 (1): 44-48.
43. Lu G, Hong W, Tong L, et al. Drying enhanced adhesion of polythiophene nanotubule arrays on smooth surfaces. *ACS Nano* 2008; 2 (11): 2342-2348.
44. Huang C, Sheng K, Qu L, et al. Dry adhesion of polythiophene nanotube arrays with drag-induced direction dependence. *Journal of Applied Polymer Science* 2012; 124 (5): 4047-4053.
45. Singh V, Bougher TL, Weathers A, et al. High thermal conductivity of chain-oriented amorphous polythiophene. *Nature Nanotechnology* 2014; 9 (5): 384-390.
46. Liu P, Ng VMH, Yao Z, et al. Ultrasmall Fe3O4 nanoparticles on MXenes with high microwave absorption performance. *Materials Letters* 2018; 229: 286-289.
47. Liang C, Song P, Ma A, et al. Highly oriented three-dimensional structures of Fe3O4 decorated CNTs/reduced graphene oxide foam/epoxy nanocomposites against electromagnetic pollution. *Composites Science and Technology* 2019; 181: 107683.
48. Li Y, Huang Y, Yan L, et al. Synthesis and magnetic properties of ordered barium ferrite nanowire arrays in AAO template. *Applied Surface Science* 2011; 257 (21): 8974-8980.
49. de Faria DLA, Venâncio Silva S, de Oliveira MT. Raman microspectroscopy of some iron oxides and oxyhydroxides. *Journal of Raman Spectroscopy* 1997; 28 (11): 873-878.
50. Ho AYY, Yeo LP, Lam YC, et al. Fabrication and Analysis of Gecko-Inspired Hierarchical Polymer Nanosetae. *ACS Nano* 2011; 5 (3):1897-1906.
51. Dan S, Gu H, Tan J, et al. Transparent epoxy/TiO2 optical hybrid films with tunable refractive index prepared via a simple and efficient way. *Progress in Organic Coatings* 2018; 120: 252-259.
52. Muzzi B, Albino M, Gabbani A, et al. Star-shaped magnetic-plasmonic Au@Fe3O4 nano-heterostructures for photothermal therapy. *ACS Applied Materials & Interfaces* 2022; 14 (25): 29087-29098.
53. Bazzaoui EA, Marsault JP, Aeiyach S, et al. Resonance Raman study of polythiophene films in the doped and undoped states. Relations between spectral data and physicochemical properties. *Synthetic Metals* 1994; 66 (3): 217-224.
54. Shebanova ON, Lazor P. Raman study of magnetite (Fe3O4): laser-induced thermal effects and oxidation. *Journal of Raman Spectroscopy* 2003; 34 (11): 845-852.
55. Guo C, Hu Y, Qian H, et al. Magnetite (Fe3O4) tetrakaidecahedral microcrystals: Synthesis, characterization, and micro-Raman study. *Materials Characterization* 2011; 62 (1): 148-151.
56. Lei Z, Liu W, Xing W, et al. Developing thermal regulating and electromagnetic shielding nacre-inspired graphene-conjugated conducting polymer film via apparent Wiedemann-Franz law. *ACS Applied Materials & Interfaces* 2022; 14 (43): 49199-49211.
57. Wang W, Ma X, Shao Y, et al. Flexible, multifunctional, and thermally conductive nylon/graphene nanoplatelet composite papers with excellent EMI shielding performance, improved hydrophobicity and flame resistance. *Journal of Materials Chemistry A* 2021; 9(8): 5033-5044.
58. Du Y, Wang J, Cui C, et al. Pure carbon microwave absorbers from anion-exchange resin pyrolysis. *Synthetic Metals* 2010; 160 (19): 2191-2196.
59. Du Y, Liu W, Qiang R, et al. Shell thickness-dependent microwave absorption of core-shell Fe3O4@C composites. *ACS Applied Materials & Interfaces* 2014; 6 (15): 12997-13006.

60. Zhang X, Wang X, Lei Z, et al. Flexible MXene-decorated fabric with interwoven conductive networks for integrated joule heating, electromagnetic interference shielding, and strain sensing performances. *ACS Applied Materials & Interfaces* 2020; 12(12): 14459-14467.
61. Weng G-M, Li J, Alhabeb M, et al. Layer-by-layer assembly of cross-functional semi-transparent MXene-carbon nanotubes composite films for next-generation electromagnetic interference shielding. *Advanced Functional Materials* 2018; 28 (44): 1803360.
62. Zhang J, Kong N, Uzun S, et al. Scalable manufacturing of free-standing, strong Ti3C2Tx MXene films with outstanding conductivity. *Advanced Materials* 2020; 32 (23): 2001093.
63. Xu C, Liu P, Wu Z, et al. Customizing heterointerfaces in multilevel hollow architecture constructed by magnetic spindle arrays using the polymerizing-etching strategy for boosting microwave absorption. *Advanced Science* 2022; 9 (17): 2200804.
64. Das NC, Khastgir D, Chaki TK, et al. Electromagnetic interference shielding effectiveness of carbon black and carbon fibre filled EVA and NR based composites. *Composites Part A: Applied Science and Manufacturing* 2000; 31 (10): 1069-1081.
65. Karimi P, Ostoja-Starzewski M, Jasiuk I. Experimental and computational study of shielding effectiveness of polycarbonate carbon nanocomposites. *Journal of Applied Physics* 2016; 120 (14): 145103.
66. Liang J, Wang Y, Huang Y, et al. Electromagnetic interference shielding of graphene/epoxy composites. *Carbon* 2009; 47 (3): 922-925.
67. Nasouri K, Shoushtari AM. Fabrication of magnetite nanoparticles/polyvinylpyrrolidone composite nanofibers and their application as electromagnetic interference shielding material. *Journal of Thermoplastic Composite Materials* 2017; 31 (4): 431-446.
68. Bora PJ, Vinoy KJ, Ramamurthy PC, et al. Electromagnetic interference shielding effectiveness of polyaniline-nickel oxide coated cenosphere composite film. *Composites Communications* 2017; 4: 37-42.
69. Lu B, Dong XL, Huang H, et al. Microwave absorption properties of the core/shell-type iron and nickel nanoparticles. *Journal of Magnetism and Magnetic Materials* 2008; 320 (6): 1106-1111.
70. Zhao H, Wang F, Cui L, et al. Composition optimization and microstructure design in MOFs-derived magnetic carbon-based microwave absorbers: A review. *Nano-Micro Letters* 2021; 13 (1): 208.
71. Wang X, Lu Y, Zhu T, et al. CoFe2O4/N-doped reduced graphene oxide aerogels for high-performance microwave absorption. *Chemical Engineering Journal* 2020; 388: 124317.
72. Wang L, Li X, Shi X, et al. Recent progress of microwave absorption microspheres by magnetic-dielectric synergy. *Nanoscale* 2021; 13 (4): 2136-2156.
73. Wu M, Zhang Y, Hui S, et al. Microwave magnetic properties of Co50/(SiO2)50 nanoparticles. *Applied Physics Letters* 2002; 80 (23): 4404-4406.